SACLANTCEN MEMORANDUM
serial no.: SM-318

SACLANT UNDERSEA
RESEARCH CENTRE
MEMORANDUM

BROADBAND ACOUSTIC INTENSITY FLUCTUATIONS IN THE TYRRHENIAN SEA

T. Akal and B.J. Uscinski

November 1996

Report no. changed (Mar 2006): SM-318-UU

SACLANT Undersea Research Centre
Viale San Bartolomeo 400
19138 San Bartolomeo (SP), Italy

tel: +39-187-540.111
fax: +39-187-524.600

e-mail: library@saclantc.nato.int

NORTH ATLANTIC TREATY ORGANIZATION

Broadband acoustic transmission intensity fluctuations in the Tyrrhenian Sea

T. Akal and B.J. Uscinski

The content of this document pertains to work performed under Project 05 of the SACLANTCEN Programme of Work. The document has been approved for release by The Director, SACLANTCEN.

Jan L. Spoelstra
Director

intentionally blank page

Broadband acoustic intensity fluctuations in the Tyrrhenian Sea

T. Akal and B.J. Uscinski*

Executive Summary: Active sonar systems are adversely affected by random fluctuations in the ocean medium. The sonar system performance is degraded by random fades and variations in the signal that cannot be predicted by models that account for only deterministic effects in the water column. Random variations in the ocean medium have characteristics that depend on time and space. The spatial structure has important implications for the design of sonar systems and their subsequent performance.

In this report, a theoretical model of the ocean environment is proposed from measured oceanographic data which may explain the observed intensity of acoustic fluctuations. the model has two scales of variation: one accounts for the large-scale variation over time and the other accounts for a small-scale variation in depth. Comparison with the time scales corresponding to the expected internal wave field and tidal periods offers a possible interpretation, but there may be an alternative explanation. Knowing that the oceans exhibit scattering features of all scales, ranging from turbulence to mesoscale, the theory should have implications for the design and performance of both ASW and MCM systems. Future efforts will concentrate on the measurement and modelling of random fluctuations encountered in shallow water environments.

* Department of Applied Mathematics and Theoretical Physics, Cambridge University

intentionally blank page

Broadband acoustic intensity fluctuations in the Tyrrhenian Sea

T. Akal and B.J. Uscinski

Abstract:

An acoustic propagation experiment was carried out in the Tyrrhenian Sea in October 1985 in which signals from a broadband source were recorded at a range of 5 km with a vertical 62 m hydrophone array over a period of 5 days. The experiment, named 'NAPOLI 85', was designed to investigate the transfer function of the ocean medium over an acoustic frequency range from 250–2000 Hz as a function of time and position down the vertical array. This paper treats the ocean transfer function in both the time and frequency domains for the lower refracted path. The intensity fluctuations down the array at an acoustic frequency of 1 kHz are presented for the 5 days. Large fluctuations occur simultaneously over the whole extent of the array, and these can be explained by refractive effects in an intrusive later. There are also weak spatial variations down the array arising from diffractive effects in the layer. The physical mechanisms causing the time variations in the layer are not yet understood.

Keywords: Tyrrhenian Sea – propagation – sound ribbons – scattering

Contents

Broadband acoustic transmission intensity fluctuations in the Tyrrhenian Sea

B. J. Uscinski
Ocean Acoustics Group, Department of Applied Mathematics and Theoretical Physics, University of Cambridge, Silver Street, Cambridge CB3 9EW, England

T. Akal
Saclant Undersea Research Centre, La Spezia, Italy

(Received 10 February 1994; accepted for publication 11 May 1995)

An acoustic propagation experiment was carried out in the Tyrrhenian Sea in October 1985 in which signals from a broadband source were recorded at a range of 5 km with a vertical 62-m hydrophone array over a period of 5 days. The experiment, named "NAPOLI 85," was designed to investigate the transfer function of the ocean medium over an acoustic frequency range from 250–2000 Hz as a function of time and position down the vertical array. This paper treats the ocean transfer function in both the time and frequency domains for the lower refracted path. The intensity fluctuations down the array at an acoustic frequency of 1 kHz are presented for the 5 days. Large fluctuations occur simultaneously over the whole extent of the array, and these can be explained by refractive effects in an intrusive layer. There are also weak spatial variations down the array arising from diffractive effects in the layer. The physical mechanisms causing the time variations in the layer are not yet understood. © *1996 Acoustical Society of America.*

PACS numbers: 43.30.Re [JHM]

INTRODUCTION

An acoustic transmission experiment (referred to as NAPOLI 85) was carried out in the Tyrrhenian Sea, one of the major basins of the Western Mediterranean, in October 1985 in order to investigate the spatial structure of intensity variations in the propagating sound field. Many other major acoustic propagation experiments (see for example Ewart,[1] Ewart and Reynolds,[2,3] and Ellinthorpe[4]) recorded with one or two receivers over a period of several days. They thus provided much information about the behavior of the acoustic field with time but not about its spatial structure. In NAPOLI 85 the signal was recorded over five days with a 64-m vertical array of hydrophones, allowing its structure in both space and time to be studied.

Comprehensive environmental measurements were made during the acoustic transmissions, on the basis of which a model of the irregular ocean medium was constructed and theoretical predictions made concerning the expected behavior of the acoustic signal. Details of the experiment have already been reported by Uscinski *et al.*[5] together with preliminary results and an arrival-time analysis. The present paper gives a fuller description of the experimental results after data processing, particular emphasis being placed on the ocean transfer function and the intensity fluctuations. Theoretical predictions, involving the effects of both refraction and diffraction, are compared with experimental results for the intensity fluctuations.

Section I gives relevant details of the trial and Sec. II a brief summary of the data processing. The processed experimental results are presented in Sec. III while Sec. IV is an account of the intensity fluctuation theory describing this trial. Section V compares theoretical predictions with experimental results and draws some conclusions.

I. THE EXPERIMENT

A full description of the sea trial can be found in Ref. 5. The main features are as follows. Broadband acoustic signals generated by small (2.75 g TNT) electrically detonated explosive charges at a depth of 400 m were recorded by two hydrophone arrays. The first of these was a reference array with four hydrophones (at depths of 10, 85, 160, and 308 m) moored close to the source which recorded the signal before significant distortion due to the ocean had occurred (the signature). The second array recorded the signal at a distance of some 5 km from the source (the response). This array was a vertical array consisting of 32 hydrophones with a regular 2 m spacing, the top hydrophone being at a depth of 224 m.

It was subsequently found that of the 32 hydrophones in the receiving array only 26 produced reliable output. There was a total of 190 detonations (events) carried out over a period of five days. The intervals between events were 60 min on the first and fifth days, 15 min on the second day and 30 min on the third and fourth days. Simultaneous oceanographic measurements were made with moored thermistor chains and a towed oscillating body capable of providing continuous CTD measurements over a depth band from 25 to 250 m, both in the direction of acoustic transmissions as well as in the transverse direction. Finally, 4 CTD and some 70 XBT casts also gave much useful information. The oceanographic observations have been fully reported by Potter.[6,7] They have been used to determine the sound-speed profile and have allowed a direct estimate to be made of the scale sizes and spatial autocorrelation function of the ocean inhomogeneities during the trial.[5] The aim of the experiment was to calculate the ocean transfer function (the acoustic response of the ocean when the input signal is an impulse) by deconvolution of response with signature, thus permitting the

because the left-hand side of the equation must be positive semidefinite due to the squared terms. By straight forward algebraic manipulation of relation (E10) it can be shown that

$$\mathcal{J}_{\text{joint}}(a) \geq \mathcal{J}_{\text{average}}(a), \tag{E11}$$

where equality holds when the W_i are identically distributed. The joint measurements of the D intensities W_i, therefore, contain more information than a single measurement of average intensity κ unless the intensities are identically distributed, in which case the joint measurements and average have equal information. More generally, the left-hand side of relation (E10) divided by

$$\sum_{k=1}^{D} \frac{\langle W_k \rangle^2}{\mu}, \tag{E12}$$

gives the information about parameter a that is lost by keeping the average rather than the joint measurements.

Finally, by letting $\langle W_i \rangle = \bar{I}_i$, $D=S$, $\mu=1$, and then comparing Eq. (E9) with Eq. (E3), one can see that information is always gained by measuring the instantaneous intensities of the S independent fields separately and then averaging them, rather than by first measuring the intensity of the superposed fields and then dividing by S. Although this gain of information can be substantial, it requires the ability to measure the intensity of each independent field z_i separately, which is not always possible for the reasons given in Sec. III B.

[1] P. G. Bergmann, "Intensity Fluctuations," in *The Physics of Sound in the Sea, Part 1: Transmission* (National Defense Research Committee, Washington, DC, 1946).

[2] J. W. Goodman, *Statistical Optics* (Wiley, New York, 1985).

[3] P. Swerling, "Probability of detection for fluctuating targets," Rand Report RM-1217 (1954); reissued in Trans. IRE Prof. Group Inf. Theory **IT-6**, 269–308 (1960).

[4] R. Barakat, "First order probability densities of laser speckle patterns observed through finite size scanning apertures," Opt. Acta **20**, 729–740 (1973).

[5] T. Kailath, "Correlation detection of signals perturbed by a random channel," Trans. IRE Prof. Group Inf. Theory **IT-6**, 361–366 (1960).

[6] P. N. Mikhalevsky, "Envelope statistics of a partially saturated process," J. Acoust. Soc. Am. **72**, 151–158 (1982).

[7] I. Dyer, "Statistics of distant shipping noise," J. Acoust. Soc. Am. **53**, 564–570 (1973).

[8] I. Dyer and G. W. Shepard, "Amplitude and phase fluctuation periods for long-range propagation in the ocean," J. Acoust. Soc. Am. **61**, 937–942 (1977).

[9] P. N. Mikhalevsky and I. Dyer, "Approximations to distant shipping noise statistics," J. Acoust. Soc. Am. **63**, 732–738 (1978).

[10] P. N. Mikhalevsky, "First-order statistics for finite bandwidth multipath signals with and without frequency or phase modulation," J. Acoust. Soc. Am. **66**, 751–762 (1979).

[11] P. N. Mikhalevsky, "Crossing rate statistics for finite bandwidth or modulated multipath signals," J. Acoust. Soc. Am. **67**, 812–815 (1980).

[12] I. Dyer, "Statistics of sound propagation in the ocean," J. Acoust. Soc. Am. **48**, 337–345 (1970).

[13] M. Born and E. Wolf, *Principles of Optics* (Pergamon, New York, 1980).

[14] N. C. Makris, L. Avelino, and R. Menis, "Deterministic reverberation from ocean ridges," J. Acoust. Soc. Am. **97**, 3547–3574 (1995).

[15] P. M. Ogden and F. T. Erskine, "Surface and volume scattering measurements using broadband explosive charges in the Critical Sea Test 7 experiment," J. Acoust. Soc. Am. **96**, 2908–2920 (1994).

[16] L. Mandel, "Fluctuations of photon beams: The distribution of photoelectrons," Proc. Phys. Soc. **74**, 233–243 (1959).

[17] A. V. Oppenheim and R. W. Schafer, *Digital Signal Processing* (Prentice-Hall, Englewood Cliffs, 1975).

[18] H. L. Landau and H. O. Pollack, "Prolate spheroidal wave functions, Fourier analysis and uncertainty-III: The dimension of the space of essentially time- and band-limited signals," Bell Syst. Tech. J. **41**, 1295–1336 (1962).

[19] S. O. Rice, "A statistical analysis of random noise," Bell Syst. Tech. J. **24**, 46–108 (1945).

[20] P. H. Dahl and O. A. Mathisen, "Measurement of fish target strength and associated directivity at high frequencies," J. Acoust. Soc. Am. **73**, 1205–1211 (1982).

[21] J. W. Strohbehn, "Line-of-sight wave propagation through the turbulent atmosphere," Proc. IEEE **56**, 1301–1317 (1968).

[22] J. W. Strohbehn, "Modern theories in the propagation of optical waves in a turbulent medium," in *Laser Beam Propagation in the Atmosphere*, edited by J. W. Strohbehn (Springer-Verlag, New York, 1978).

[23] W. M. Siebert, *Circuits, Signals and Systems* (MIT, Cambridge, MA, 1986), p. 116.

[24] W. Wong and H. Norwich, "Obtaining equal loudness contours from Weber fractions," J. Acoust. Soc. Am. **97**, 3761–3767 (1995).

[25] N. C. Makris, "A foundation for logarithmic measures of fluctuating intensity in pattern recognition," Opt. Lett. **20**, 2012–2014 (1995).

[26] N. C. Makris, "Optimal pattern recognition in signal-dependent noise as a possible basis for the Weber–Fechner Laws," J. Acoust. Soc. Am. **98**, 2907 (A) (1995).

[27] I. S. Gradshteyn and I. M. Ryzhik, *Table of Integrals, Series and Products* (Academic, San Diego, CA, 1980).

[28] N. C. Makris and J. M. Berkson, "Long range backscatter from the Mid-Atlantic Ridge," J. Acoust. Soc. Am. **95**, 1865–1881 (1994).

[29] H. H Arsenault and G. April, "Properties of speckle integrated with a finite aperture and logarithmically transformed," J. Opt. Soc. Am. **66**, 1160–1163 (1976).

[30] J. W. Goodman, "Some effects of target induced scintillation on optical radar performance," Proc. IEEE **53**, 1688–1700 (1965).

[31] A. D. Pierce, *Acoustics* (Acoustical Society of America, Woodbury, NY, 1991).

[32] H. Bateman and Staff of the Bateman Manuscript Project, *Tables of Integral Transforms* (McGraw-Hill, New York, 1954). In this reference, there are apparently some sign errors in the integral transforms necessary to compute the intensity-rate distribution of Sec. 5. These are corrected in the 1980 version of Gradshteyn and Ryzhik, Ref. 27.

[33] The random variable W for integrated intensity has accidently been omitted from the argument of the modified Bessel function in Eq. (6.1–34) of Ref. 2.

[34] B. K. P. Horn and E. J. Weldon, Jr., "Direct methods for recovering motion," Int. J. Comput. Vision **2**, 51–76 (1988).

[35] P. J. Davis and I. Polonsky, "Numerical interpolation, differentiation and integration," in *Handbook of Mathematical Functions*, edited by M. Abramowitz and I. A. Stegun (National Bureau of Standards, Washington, DC, 1964).

[36] C. R. Rao, *Linear Statistical Inference and Its Applications* (Wiley, New York, 1966).

[37] N. C. Makris, "Parameter resolution bounds that depend on sample size," J. Acoust. Soc. Am. **99**, 2851–2861 (1996).

[38] R. A. Fisher, *Statistical Methods and Scientific Inference* (Hafner, New York, 1956).

[39] R. A. Fisher, "Theory of statistical estimation," Proc. Cambridge Philos. Soc. **22**, 700–725 (1925).

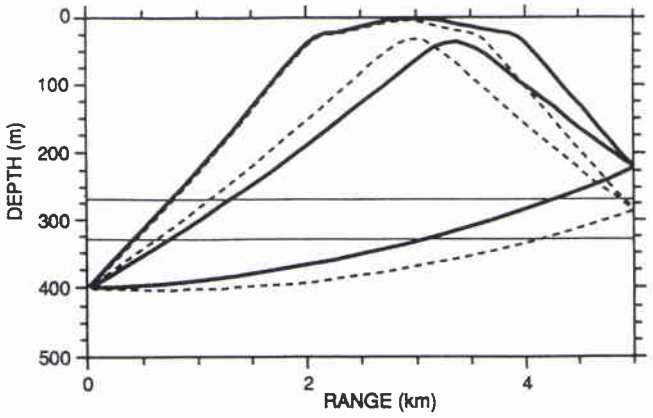

FIG. 1. Principal eigenrays to the top and bottom hydrophones of the array. The band indicates the position of the intrusive layer where the random inhomogeneities are stronger.

acoustic intensity to be determined as a function of depth and time over a range of acoustic frequencies.

A. Ray theory predictions

Eigenrays from the source to the top and bottom hydrophones of the receiving array, calculated on the basis of the measured sound-speed profile, are shown in Fig. 1. There are three paths connecting the source to the receiver, a lower direct path, an upper refracted path and an upper reflected path with intensities in the ratio 1.0: 1.4: 0.18 for the top hydrophone, and 1.01: 1.40: 0.33 for the bottom hydrophone. The upper refracted path arrives 20–30 m s after the direct path and the upper reflected path arrives 0.2–2 m s before the upper refracted path with the separation of the pulses increasing as the depth decreases.

The ray paths are determined by the mean sound speed. There are, however, superimposed sound-speed inhomogeneities of smaller scale throughout the depth of the water column. The oceanographic measurements revealed the presence of a layer between 270 and 330 m, within which the strength of the random inhomogeneities was significantly higher. This layer is also shown in Fig. 1.

B. Acoustic measurements

The signature recorded at the reference array and the corresponding response recorded at the top hydrophone of the receiving array for a typical event are shown in Fig. 2. The pulses corresponding to the three paths can be seen clearly in the response. The predictions from ray theory enable us to associate the first pulse with the lower refracted path, the second weak pulse with the upper reflected path and the third pulse with the upper refracted path. The time origin in Fig. 2 is chosen so that it corresponds with the arrival time of the first pulse. The arrival time varies from hydrophone to hydrophone down the array and a detailed analysis of arrival-time results for the direct path is given in Ref. 5. In the remainder of this paper we shall be concerned with intensity fluctuations associated with the direct path only. There is no

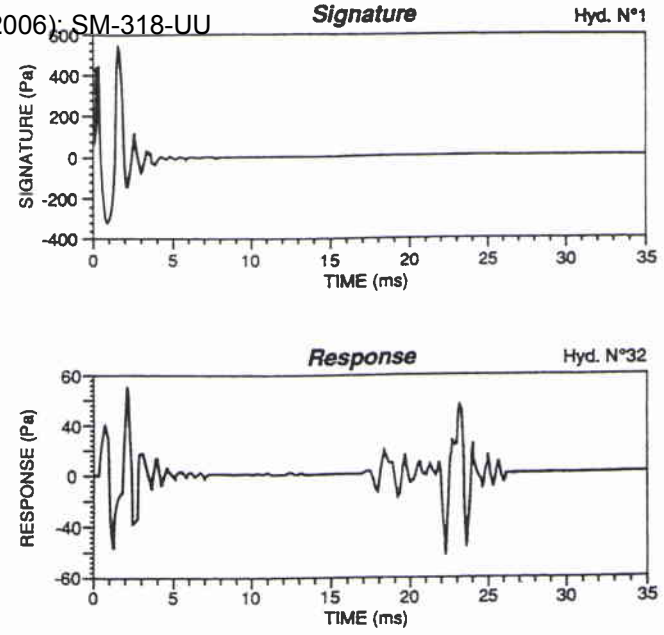

FIG. 2. Signature and response for the bottom hydrophone in the reference array and the top hydrophone in the receiving array.

reflection along the lower refracted path and it does not pass through a caustic. This allows a powerful non-negativity constraint to be used in the deconvolution procedure.

As mentioned in Ref. 5 the position of the source with respect to the arrays varied during the experiment. However, each time a transmission was made the ship was manouvered as close as possible to the same position, and the bearing and distance of each array was obtained from the ship's radar and logged. These results were used to correct the intensity of each pulse at each array for the gross geometric spreading effect.

II. DATA PROCESSING

Details of how the acoustic signals were filtered and recorded are given in Ref. 5, together with the method used to estimate the fluctuations of relative arrival times down the array due to the random structure of the ocean medium. The same random structures also cause variations in acoustic intensity, and a different form of data processing was needed to study these effects. The procedures adopted are described fully elsewhere and only a brief outline is given here.

The signature $s(t)$ of an individual event (No. 30) is shown in Fig. 3(a) and (b) together with $|S(\omega)|$ the modulus of its Fourier transform $S(\omega)$

$$\hat{s}(\omega)=\frac{1}{2\pi}\int s(t)e^{-i\omega t}\,dt. \tag{1}$$

Here $S(\omega)$ corresponds to the frequency spectrum of the signature. The response $r(t)$ of the same event is shown in Fig. 3(c),(d) together with its Fourier transform $\hat{r}(\omega)$. Comparison of the moduli of the Fourier transforms of signature [Fig. 3(b)] and response [Fig. 3(d)] reveal marked frequency differences above about 2 kHz. While this is partly due to the

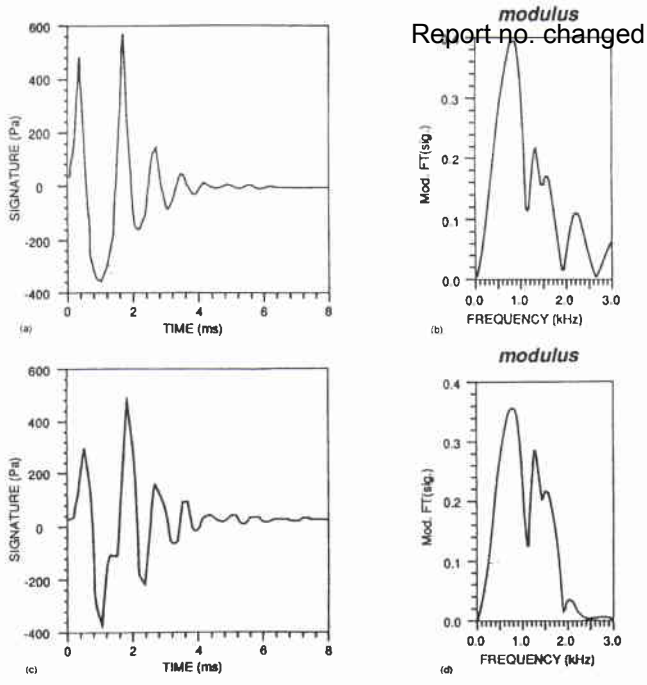

FIG. 3. (a) Lower refracted path signature. (b) Modulus the Fourier transform of the signature. (c) Lower refracted path response. (d) Modulus of the Fourier transform of the response.

medium, some of the difference is also due to the fact that received and transmitted signals were filtered with different hardware filters having different characteristics. These, however, were unchanged during the experiment. It is the pulse to pulse variation of the transfer function over the five days that is of interest and this is independent of the filter difference. Since $s(t)$, $\hat{s}(\omega)$ are known we can allow for the variations of signature intensity over the different frequencies and thus extract the fluctuation effects in the response due to ocean inhomogeneities. Signature and response are assumed to be related by the convolution

$$r(t)=\int_{-\infty}^{\infty} K(t')s(t-t')dt'+\epsilon(t), \tag{2}$$

where $K(t)$ is sometimes called the ocean impulse response function and is the response that would be received if the input signature were a Dirac delta function, and $\epsilon(t)$ includes the noise present in the system and the ocean.

The frequency content of $K(t)$ is given by its Fourier transform $\hat{K}(\omega)$ and we see from (2) that the spectra $\hat{s}(\omega)$, $\hat{r}(\omega)$ are related by

$$\hat{r}(\omega)=\hat{K}(\omega)\hat{s}(\omega)+\bar{\epsilon}(\omega), \tag{3}$$

where $\bar{\epsilon}(\omega)$ is the Fourier transform of the noise term. The simplest estimate of $\hat{K}(\omega)$ is found by forming $\hat{r}(\omega)/\hat{s}(\omega)$ and omitting $\bar{\epsilon}(\omega)$. This method is subject to severe limitations, breaking down when $\hat{s}(\omega)$ passes through zero or becomes very small. An example of $\hat{K}(\omega)$ estimated in this way is shown in Fig. 4. Despite the limitations of this approach the $\hat{K}(\omega)$ thus obtained provide useful information concerning the origins of the intensity fluctuations.

Overcoming the above limitations means deconvolving Eq. (2). The mathematical problem of deconvolution is, in general, ill posed but for some types of signal the problem can be solved if certain assumptions about the properties of the solution are known to apply. In particular, if it is known that the transmitted signals are reasonably broadband and that none of the paths deliver the signal with a reversed phase (which constrains the ocean transfer function to be positive) and if, in addition, an estimate of the maximum width of K is available, then identification of the ocean transfer function can be achieved. Two methods were used to deconvolve the signature and response. The first of these, described in detail in Refs. 8–11 make extensive use of available nonlinear physical constraints aiming to restore as much information as possible, particularly at the higher frequencies. It allows for dispersion but introduces up to 25% bias into the estimate of K. The impulse response function $K(t)$ for event No. 9 found by this method is shown in Fig. 5 for the top and bottom hydrophones. The modulus and phase of the corresponding spectra $\hat{K}(\omega)$ are shown in Fig. 6. The value of $|\hat{K}(\omega)|^2$ gives the intensity in the range ω to $\omega+\Delta\omega$ independently of the variations due to the signature. The general form of the transfer function in Figs. 4 and 6 is seen to differ somewhat. This is chiefly due to the fact that $K(\omega)$ in Fig. 4 was got by the simplest of methods, neglecting noise and making no allowance for dispersion and variation in width of the impulse response function.

The second of the methods used[12] is similar in some respects, but makes less use of physical constraints. Namely, it is based on the assumption that linear ray theory applies and hence there is no disperson. As a result it has a smaller bias but it does not provide an estimate of the changing width of the ocean transfer function throughout the experiment (see discussion in Ref. 11).

III. EXPERIMENTAL RESULTS

By plotting

$$|\hat{K}(\omega)|^2=I(\omega) \tag{4}$$

for each hydrophone the acoustic intensity down the receiving array can be studied over the entire experiment for a selected acoustic frequency $\omega=2\pi f$. The result is shown in Fig. 7 for $f=1000$ Hz. Similar patterns are obtained at other frequencies, for example $f=2000$ Hz. The most obvious features are the large-scale deep modulations over time that appear to affect all the hydrophones simultaneously, and the fine-scale shallow modulations down the array.

Let the intensity at the mth hydrophone for the nth event be $I_{n,m}$. Let angle brackets denote an average over time and an overbar denote an average over depth. The average intensity-depth profile is then

$$\langle I\rangle_m=\frac{1}{N}\sum_{n=1}^{N} I_{m,n}, \tag{5}$$

where $N=190$ is the number of events. This profile is shown in Fig. 8 and reflects the constant intensity bias down the array due to differences in hydrophone performance.

The average intensity-time profile is

$$\overline{I_n}=\frac{1}{M}\sum_{m=1}^{M} I_{m,n}, \tag{6}$$

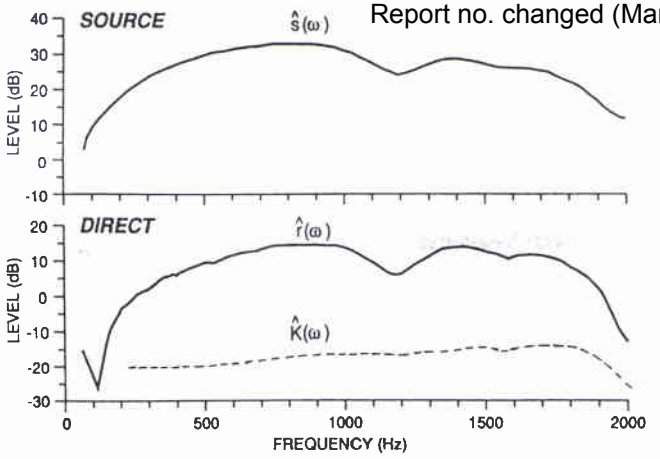

FIG. 4. The spectra $\hat{s}(\omega)$ and $\hat{r}(\omega)$ of the intensity fluctuations at a single hydrophone, for the direct path. The direct estimate of $\hat{K}(\omega)$ is also shown.

where $M=26$ is the number of good hydrophones. This profile is shown in Fig. 9.

A. Deterministic effects

This paper aims to study intensity fluctuations caused by the irregular ocean medium. For this reason any deterministic changes down the array or possible variations due to differences in performance of individual hydrophones need to be removed. These spatially deterministic effects are given by

$$\langle \Delta I \rangle_m = \langle I \rangle_m - \langle \bar{I} \rangle, \tag{7}$$

where

$$\langle \bar{I} \rangle = \frac{1}{NM} \sum_{n=1}^{N} \sum_{m=1}^{M} I_{m,n} \tag{8}$$

is the space-time mean of intensity and has a value of 0.185×10^{-1}. The new intensity $\mathcal{I}_{m,n}=\mathcal{I}(z,t)$, defined as

$$\mathcal{I}_{m,n} = I_{m,n} - \langle \Delta I \rangle_m, \tag{9}$$

removes the deterministic variations leaving those fluctuations due to the ocean medium. A plot of $\mathcal{I}_{m,n}$ has an appearance almost identical to that of $I_{m,n}$ in Fig. 7 and so will not be presented again.

B. Fluctuations in time

On averaging the new intensity $\mathcal{I}_{m,n}$ over space we regain the average intensity-time profile

$$\mathcal{I}(t) = \frac{1}{M} \sum_{m=1}^{M} I_{m,n} = \bar{I}_n. \tag{10}$$

A measure of the large time scale fluctuations of intensity, Fig. 7, is the normalized variance of $\mathcal{I}(t)$

$$S_t^2 = (\langle \mathcal{I}^2(t) \rangle - \langle \mathcal{I}(t) \rangle^2) / \langle \mathcal{I}(t) \rangle^2, \tag{11}$$

sometimes called the scintillation index. For this trial

$$S_t^2 = 0.377. \tag{12}$$

This level could be regarded as appreciable but not large.

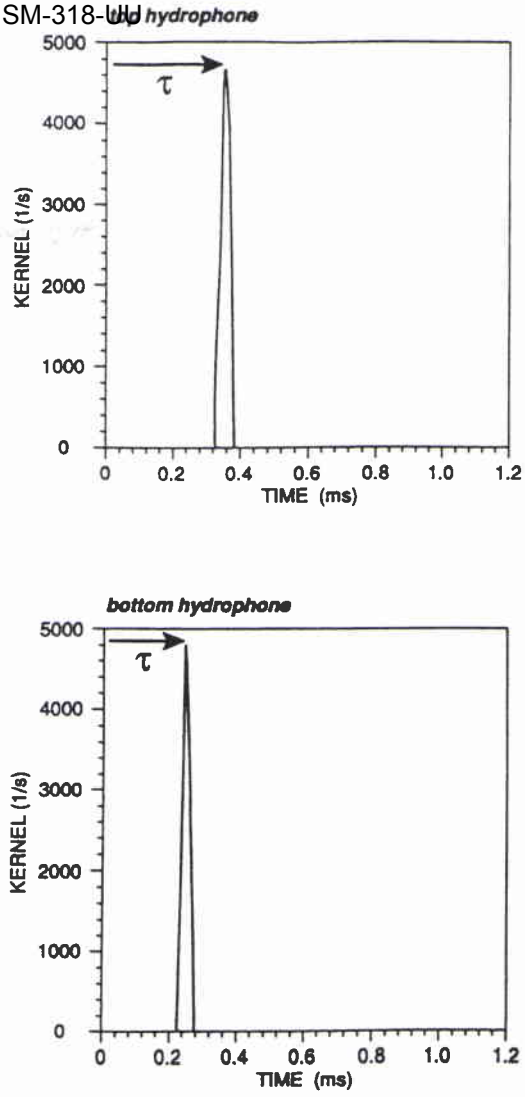

FIG. 5. Impulse response function for event number 9. The time delay τ is subtracted before the calculation of the Fourier transform.

Another quantity of interest is the autocorrelation of $\mathcal{I}(t)$.

$$R(t_1-t_2) = (\langle \mathcal{I}(t_1)\mathcal{I}(t_2) \rangle - \langle \mathcal{I} \rangle^2) / (\langle \mathcal{I}^2 \rangle - \langle \mathcal{I} \rangle^2). \tag{13}$$

This is shown in Fig. 10. The same quantity can also be estimated by averaging in a different order. Starting from $\mathcal{I}_{mn}$ the time correlation can be formed for each hydrophone down the array, then averaged over depth. The two results are almost identical. The autocorrelation function shown in Fig. 10(a) was obtained by processing the data by the methods of Ref. 12, while that in Fig. 10(b) resulted from the methods of Refs. 8–11. The two are similar in appearance but the time scale of the variation in Fig. 10(a) appears somewhat longer than that of Fig. 10(b). The time autocorrelation of Fig. 10 bears a resemblance to the spatial autocorrelation of irregular structure in the ocean obtained from the T.O.B. data and presented in Ref. 6 (Figs. 7 and 8). This, however, does not necessarily imply that the two are connected.

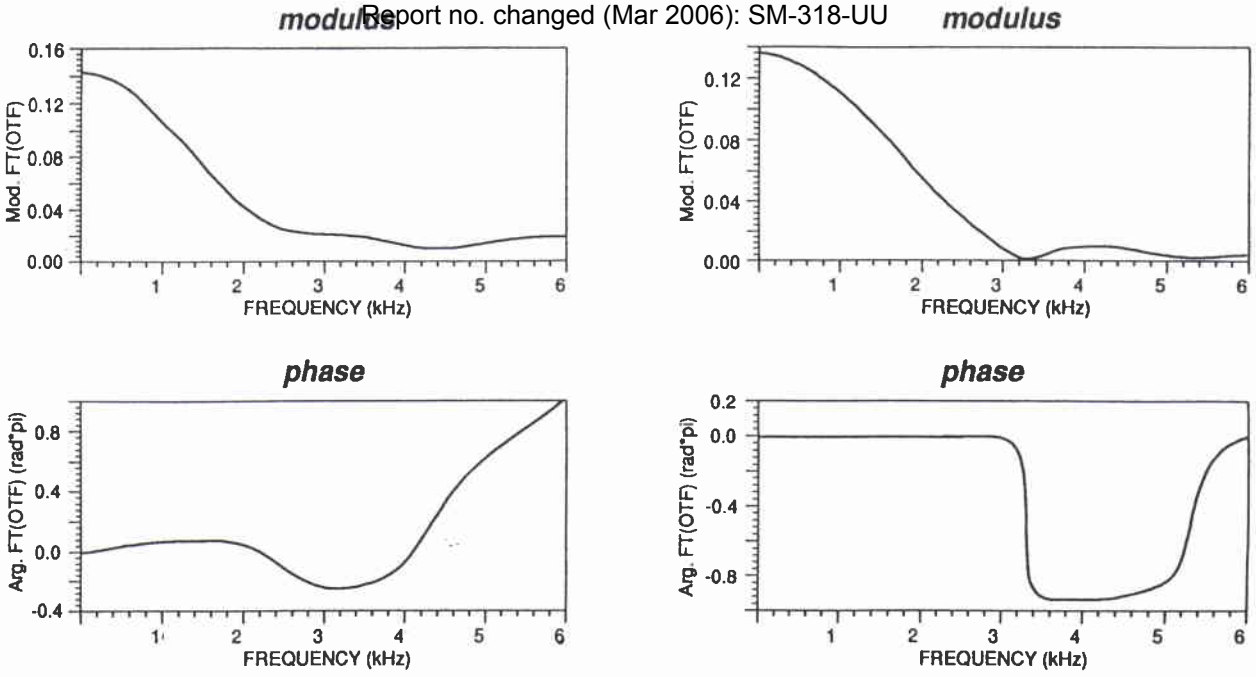

FIG. 6. Modulus and phase of the Fourier transform of the impulse response function at the top and bottom hydrophones in the receiving array for event number 9.

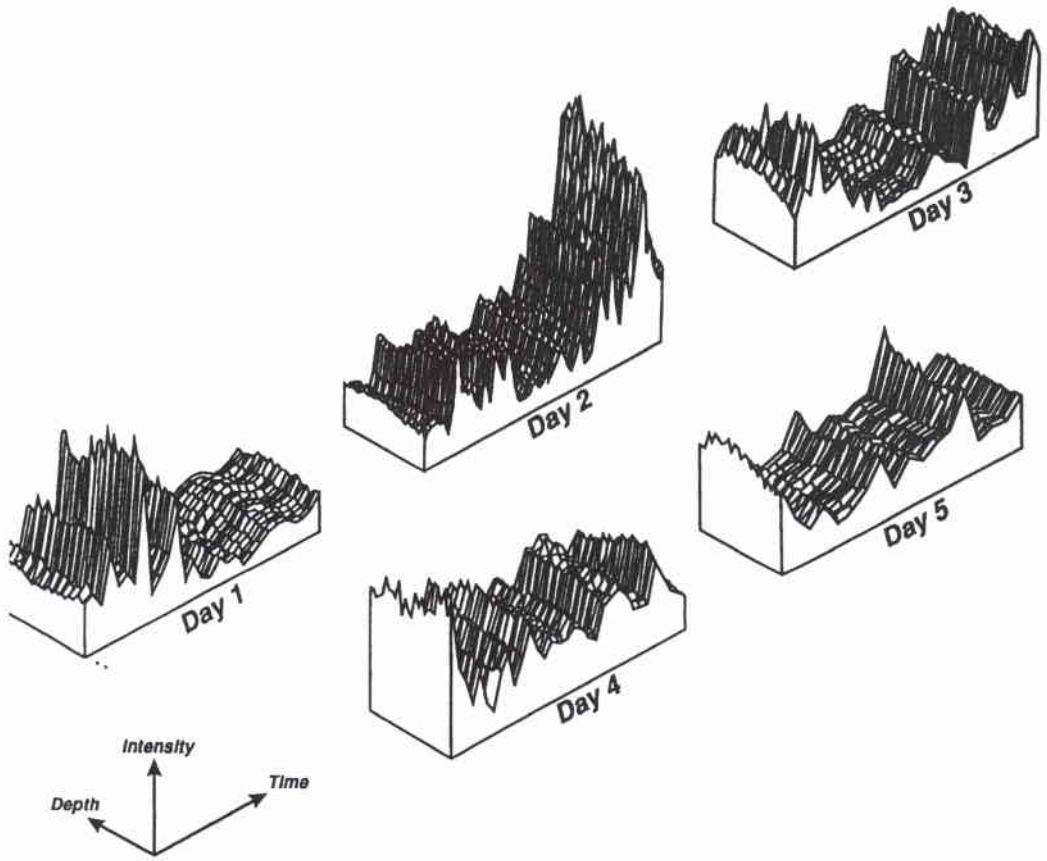

FIG. 7. Surface plots of intensity against time and depth for the entire experiment. The acoustic frequency is 1000 Hz. The intensity axis ranges from 0.0 to 0.07.

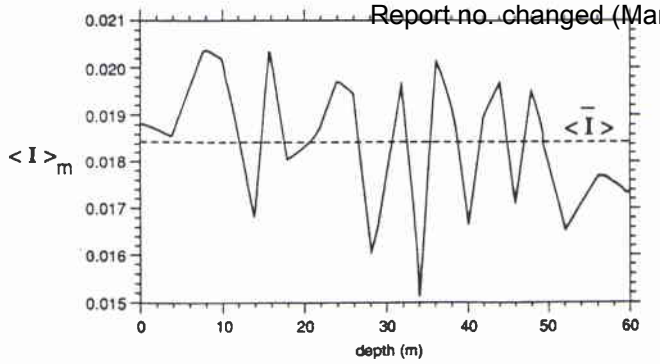

FIG. 8. Acoustic intensity at a frequency of 1000 Hz averaged over the five days of the experiment versus depth. This shows the constant intensity bias down the array due to differences in hydrophone performance.

1. Probability density of $\mathscr{I}(t)$

The intensity-time profile $\mathscr{I}(t)$ (Fig. 7) can be used to estimate the experimental probability density of the large scale intensity variations. The intensities are first normalized by defining

$$J(t)=\mathscr{I}(t)/\langle\mathscr{I}\rangle, \tag{14}$$

so that

$$\langle J(t)\rangle=1. \tag{15}$$

The interval $[J_{\min},J_{\max}]$ is split into B bins, the number of times $J(t)$ lies between J_b and J_{b+1} calculated and divided by the total number of observations to give the probability distribution, then divided by the bin size to give the normalized probability density. The experimental probability density for $B=40$ is shown in Fig. 11 with the smooth curve of best fit.

C. Fluctuations in space

To study the spatial structure of intensity fluctuations down the array we revert to $\mathscr{I}(z,t)$, Eq. (9), and form its variance for each event separately, taking spatial averages. We then average over all the events and form the spatial version of the scintillation index:

$$S_z^2=\langle(\overline{\mathscr{I}^2}(z,t)-\bar{\mathscr{I}}(z,t)^2)\rangle/\langle\bar{\mathscr{I}}(z,t)^2\rangle. \tag{16}$$

For this trial

$$S_z^2=0.18\times10^{-2}. \tag{17}$$

On comparing with Eq. (12) we see that the fine scale spatial variations of intensity down the array are much smaller than large scale time fluctuations.

Finally, the autocorrelation function of the fine scale spatial structure is formed in a similar manner

$$R(z_1-z_2)=\langle\overline{\mathscr{I}(z_1,t)\mathscr{I}(z_2,t)}-\overline{\mathscr{I}(z,t)^2}\rangle/\langle(\overline{\mathscr{I}^2}-\bar{\mathscr{I}}^2)\rangle. \tag{18}$$

This is shown in Fig. 12.

IV. THEORY

Oceanographic measurements made during the course of the trial are described and analysed in Refs. 5–7. These measurements indicate that the acoustic refractive index profile $n(z)$ contained an intrusive layer between about 270 and 330 m. In order to model such a layer of thickness $2d$ centered on $z=z_0$ the profile is written as follows:

$$\begin{aligned} n(x,y,z,t)&=n_0(z)+\eta_1 n'(x,y,z,t) \quad (z<z_0-d)\\ &=n_0(z)-\tfrac{1}{2}c(t)\{d^2-(z_0-z)^2\}n'(x,y,z,t)\\ &\quad (z_0+d<z<z_0-d)\\ &=n_0(z)+\eta_3 n'(x,y,z,t) \quad (z>z_0+d). \end{aligned} \tag{19}$$

In the vicinity of the layer $n_0(z)$, the mean profile is a linear function of z, $n'(x,y,z,t)$ describes the random irregularities, it has zero mean and variance unity. The measured variances of the irregular structures are[5]

$$\begin{aligned} &\eta_1^2=5\times10^{-9}, \quad 220\ \text{m}<z<270\ \text{m},\\ &\eta_2^2=1.5\times10^{-8}, \quad 270\ \text{m}<z<330\ \text{m},\\ &\eta_3^2=1\times10^{-9}, \quad 330\ \text{m}<z<400. \end{aligned} \tag{20}$$

In Eq. (19)

$$c(t)=\frac{\partial^2 n}{\partial z^2}(z,t) \tag{21}$$

is the curvature of the layer profile, it is assumed to be a Gaussian random variable with zero mean and variance σ_c^2. The variance of the refractive index in the layer is thus

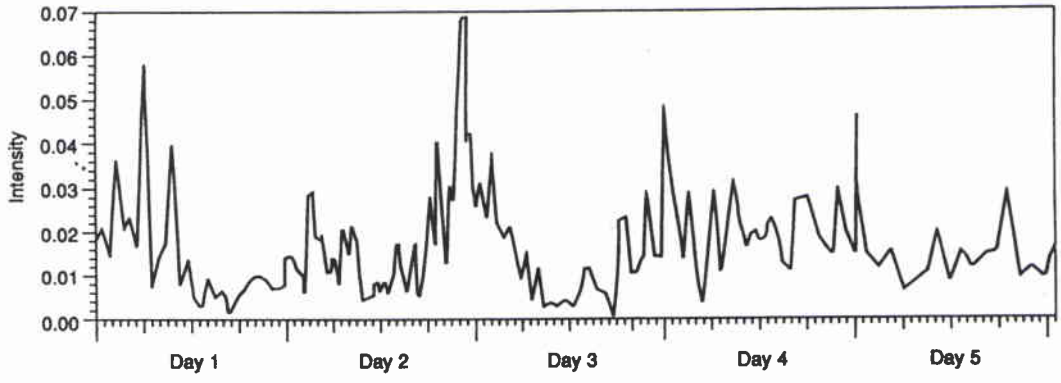

FIG. 9. Intensity averaged over depth displayed as a function of time. The frequency is 1000 Hz.

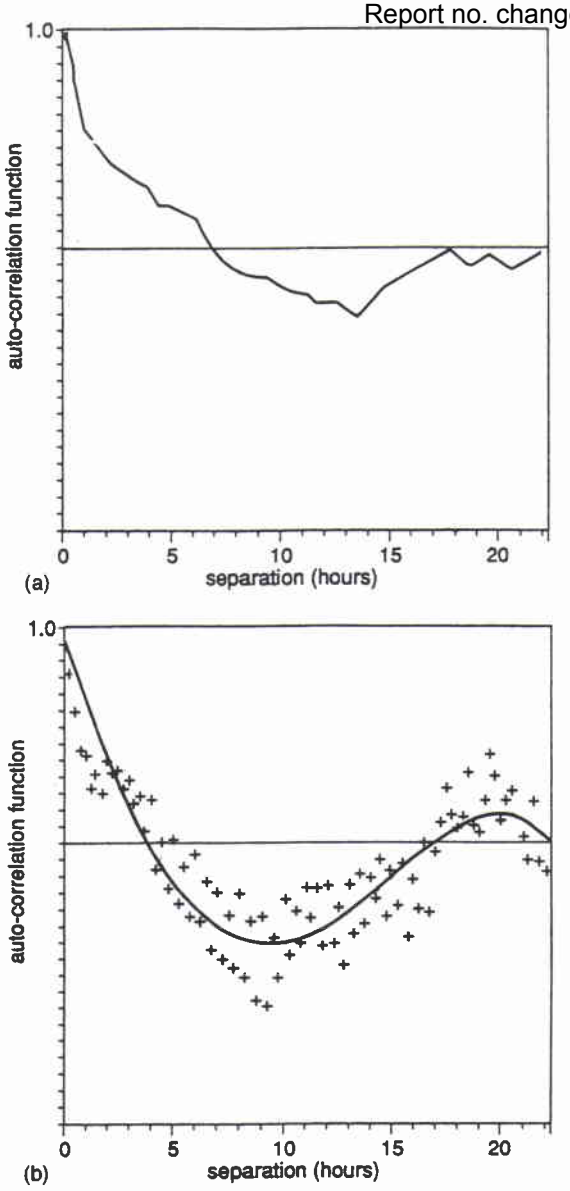

FIG. 10. (a) The autocorrelation of $\mathscr{I}(t)$, Eq. (10), from data processed by the methods of Ref. 12. (b) The autocorrelation of $\mathscr{I}(t)$ as a function of time separation. The marked points are the measured values. The smooth curve is a weighted least-squares fourth-order polynomial best fit. Data processed by the methods of Refs. 8–11.

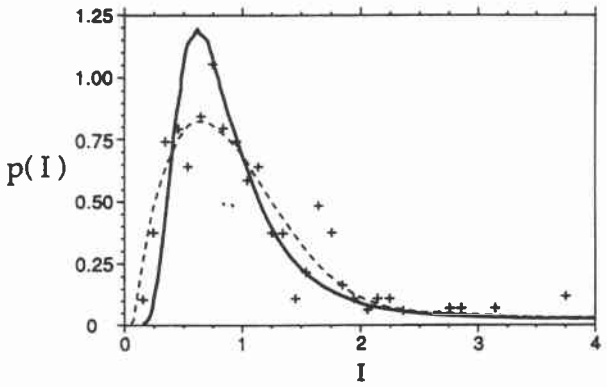

FIG. 11. The experimental probability density of $I(t)$. The crosses are the measured values and the broken curve is a least-squares sixth-order polynomial best fit. The smooth curve is the theoretical result for $\sigma_c x^2=3.0$.

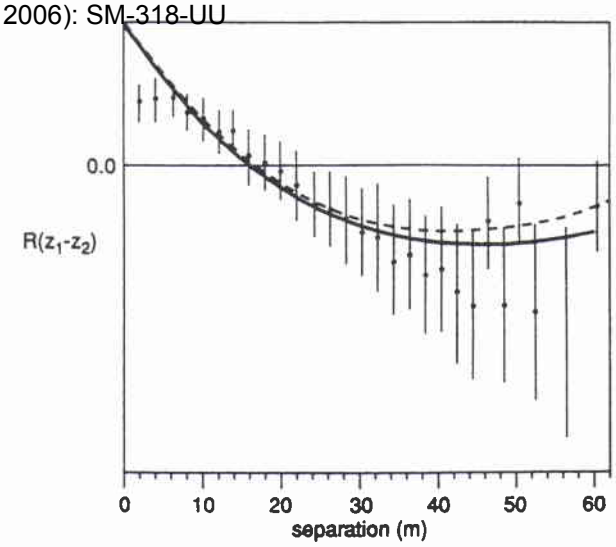

FIG. 12. The autocorrelation function $R(z_1-z_2)$, Eq. (8), of spatial variations of intensity down the array averaged over the entire experiment. The smooth curve is a weighted least-squares fourth-order polynomial best fit. The broken curve is the theoretical result of Appendix C.

$$\langle (n-n_0)^2\rangle = \frac{\sigma_c^2}{4}\,[d^2-(z_0-z)^2]^2. \tag{22}$$

The average of this variance, found by integrating through the layer, is equal to η_2^2, giving

$$\sigma_c^2 d^4 = \tfrac{15}{2}\eta_2^2. \tag{23}$$

In the theoretical analysis that follows it is assumed that the intrusive layer refracts the sound rays in such a way as to produce the large scale time variations of intensity that appear at all the hydrophones simultaneously. The small scale spatial variations observed down the hydrophone chain can be described in terms of diffraction by the random irregular structures. This approach provides an explanation for the separate large and fine scale fluctuation effects that are the most obvious feature of the depth-time intensity record (Fig. 7). They allow us to account for the two different scintillation indices corresponding to time and space variations, Eqs. (12), (17).

A. Refractive effects

The intrusive layer is assumed to act like a lens. On passing through it adjacent rays can be focused to a greater or lesser extent, depending on the curvature. Using second moment theory[13] the present simplified model of a parabolic profile is investigated in Appendix A to give approximate forms for $P(\mathscr{I}(t))$, the probability distribution of the time varying intensity Eq. (10), S_t^2 the scintillation index, and $R(t_1-t_2)$ the autocorrelation function of $\mathscr{I}(t)$.

The probability density $P(\mathscr{I})$ is given in Fig. 13 for several values of $\sigma_c x^2$. It can be shown from Eq. (A1) that the parabolic profile focuses the field for $\sigma_c x^2=\pi^2$. The curves represented are for ranges less than the focus and have been calculated by numerical evaluation of the appropriate expressions (Appendix A). An analytical form for $P(\mathscr{I})$ can also be found, Eqs. (A8), (A12) which agrees well with the full numerical form for small values of $\sigma_c x^2$.

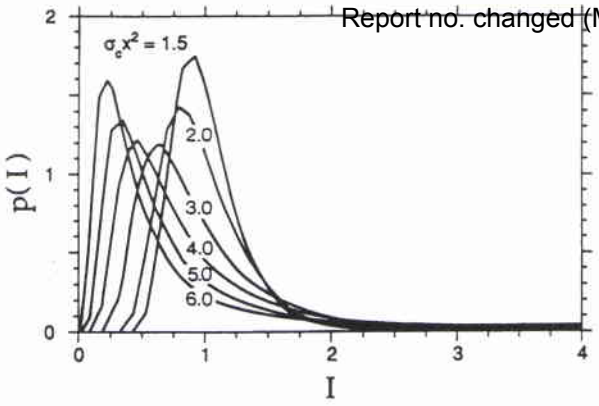

FIG. 13. Theoretical probability density calculated by the numerical method for different values of the parameter $\sigma_c x^2$.

The scintillation index, Eq. (11), evaluated numerically (Appendix A) is given in Table I for a range of values of $\sigma_c x^2$. An estimate of σ_c obtained from Eq. (23) by using the measured d and η_2^2 gives $\sigma_c \sim 4\times 10^{-7}$. The experimentally observed scintillation index S_t^2 is 0.377, which from Table I implies a $\sigma_c x^2$ of about 2.75, when

$$x \sim 2.6 \text{ km}. \tag{24}$$

Thus is about twice the slant range that would be expected from Fig. 1. However σ_c is strongly dependent on the layer thickness d and small variations in this, or in the height of the layer above the source, could bring the observations and theoretical estimates into better agreement.

The experimental probability distribution shown in Fig. 11 is most closely approximated by the theoretical form corresponding to $\sigma_c x^2 = 3.0$. Although the peak in the theoretical form is too high it is in the right position.

The above comparisons between the theory and observations indicate that the model of a parabolic refracting layer can explain most of the features of the large scale intensity fluctuations, at least quantitatively, and so deserves serious consideration in spite of the short-comings mentioned above.

B. Time autocorrelation function of intensity

This quantity $R(t_1 - t_2)$, Eq. (13), is calculated in Appendix A. Curves are given in Fig. A1 for several values of $\sigma_c x^2$ in the particular case when the autocorrelation function of the curvature

$$r(t_1 - t_2) = \langle c(t_1) c(t_2) \rangle \tag{25}$$

has the form

TABLE I. The scintillation index for a range of values of $\sigma_c x^2$.

$\sigma_c x^2$	Scintillation index
1.0	0.03
1.5	0.07
2.0	0.15
2.5	0.26
2.75	0.35
3.0	0.46
4.0	1.14
5.0	1.91

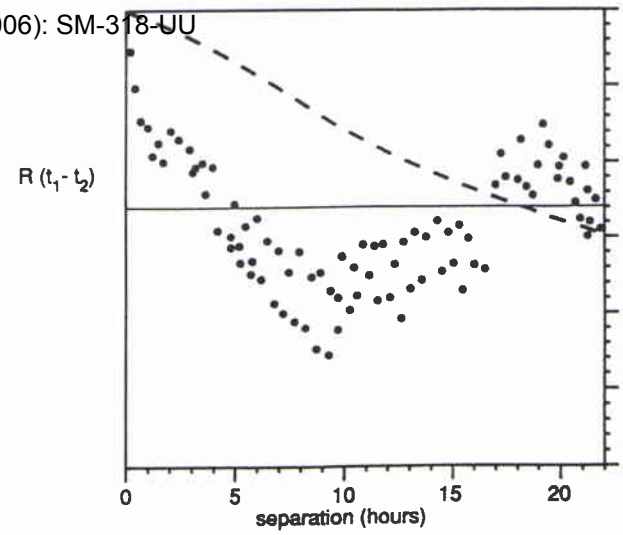

FIG. 14. The autocorrelation function $R(t_1 - t_2)$, Eq. (13), of time variations of intensity averaged down the array. The broken curve is the corresponding autocorrelation function due to a saturated internal wave field, Eq. (B3).

$$r(\tau) = e^{-\tau}(1 - 4\tau + \tau^2), \tag{26}$$

$$\tau = t_1 - t_2. \tag{27}$$

In order to compare the experimental data for $R(\tau)$ with the curve expected from a given physical process we need to know the form of $r(\tau)$ corresponding to that process. In Appendix B $r(\tau)$ for an internal wave field described by the Garrett–Munk spectrum[14] is derived. This is then used in the theory of Appendix A to give $R(\tau)$, shown in Fig. 14 together with the experimental data. The agreement is not good and so internal wave motion offers no obvious explanation of the large scale time variations of intensity at the array. The tidal cycles at the experimental site were also considered. The time spectrum of the process $\mathcal{I}(t)$ Eq. (10) obtained by the methods of Ref. 12, corresponding to the autocorrelation function of Fig. 10(a), is shown in Fig. 15. The position of a 12-h tide cycle is shown by an arrow, and is very close to an observed peak. A possible explanation could lie in some 12-h periodic forcing with an much slower random changes with a time scale of about 2 days. This latter might account for the energy at the very low end of the spectrum.

C. Diffraction effects

The main modifications of the acoustic signal occur in the intrusive layer where the ocean irregular structures are strongest. Changes in the overall curvature of this layer could spread or compress the ray path bundle as a whole, leading to the refractive changes in intensity observed simultaneously at all hydrophones. At the same time, however, the irregular structures in the layer introduce spatially random phase variations into the acoustic wavefront which then develop, into small intensity fluctuations. This leads to a variation in signal strength from hydrophone to hydrophone down the array.

In order to treat these effects we make some simplifications to the model. First, the ray paths from the source are assumed to be straight lines. This is permissible since their

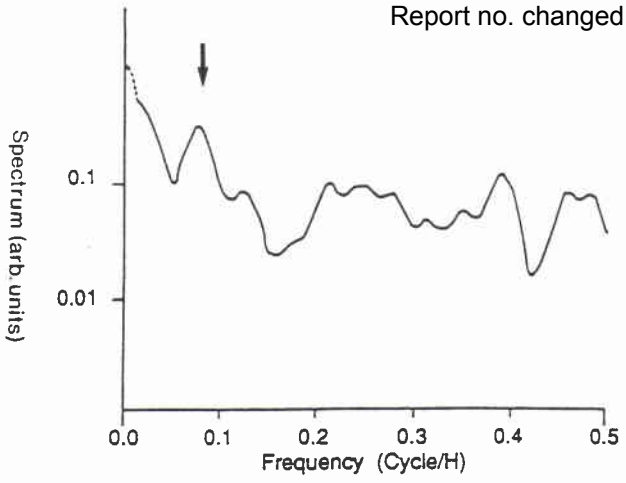

FIG. 15. The time spectrum of $\mathcal{I}(t)$, Eq. (10) with the data processed by the methods of Ref. 11. The 12-h tide period is indicated by an arrow.

curvature is very small. It simply means that the effective source is situated somewhat lower than the real one. Second, the irregular structures are all projected on to a single plane in the layer so that their effects can be regarded as those arising from a phase modulated screen. This idealized model is shown in Fig. C1.

The spatial autocorrelation function of small scale intensity fluctuations produced down the vertical array due to irregularities in the intrusive layer is derived in Appendix C on the basis of the simplified model. This theoretical autocorrelation function is shown in Fig. C3 for several values of the effective source depth. The effective depth that gives a best fit to the rays where they traverse the layer is about 550 m from the surface. Figure 12 gives the theoretical autocorrelation function for this source depth together with the experimental measurements of $R(z_1-z_2)$. The agreement in this case is reasonable.

V. CONCLUSIONS

The intensity of the acoustic signal received down the 64-m vertical array in the NAPOLI 85 transmission experiment exhibited variations in both space and time. Large time varying fluctuations of intensity over the whole extent of the array were observed. At the same time weak spatial variations occurred down the array with an inner scale of the order of 10 m. The large-scale time variations could be explained by refractive effects resulting from compression and spreading of the ray paths passing through a moderately strong intrusive layer with a changing refractive index profile. The weak spatial variations could be caused by the irregular structures present in the water column, particularly in the vicinity of the stronger layer.

The physical mechanism responsible for the time variation in the profile of the intrusive layer is not clear. Comparison with the time scales corresponding to the expected internal wave field and tidal periods offers a possible interpretation, but there might well be an alternative explanation.

ACKNOWLEDGMENTS

The authors are grateful to Professor T. E. Ewart of the Applied Physics Laboratory, University of Seattle, Dr. H. Perkins and Dr. J. Potter of the Saclant Undersea Centre, La Spezia, Italy, and Dr. L. Fradkin of the Department of Applied Mathematics and Theoretical Physics, Cambridge, U.K. for helpful discussions and advice. They also wish to thank Dr. M. Stirland of the Marconi Company U.K. for his help in interpreting the data. B. J. Uscinski was supported by the Isaac Newton Trust while writing this paper.

APPENDIX A

1. Refractive effects

Consider a ray as it enters the intrusive layer and traverses it at a shallow angle, Fig. 1. The effect of the layer on the acoustic intensity along this ray can be estimated using the analysis given by Macaskill and Uscinski.[13] If the mean intensity on entering the layer is I_0 then for shallow ray angles the intensity at a range x from the point of entry can be shown to be

$$I(t)=I_0|x\sqrt{|c|}/\sin(x\sqrt{|c|}|), \quad c(t)<0,$$
$$=I_0|x\sqrt{|c|}/\sinh(x\sqrt{|c|})|, \quad c(t)>0, \tag{A1}$$

where c is the curvature of the parabolic profile.

2. The probability density

The units in which the intensity is measured can be specified so that $\langle I(t)\rangle=1$. In this case the above quantity $I(t)$ corresponds to the normalized intensity $J(t)$, Eq. (14), whose experimental probability density was estimated. The theoretical probability density $P(I(t))$ can be found from (A1) on the assumption that $c(t)$ obeys the normal distribution

$$p(c)=\frac{1}{\sigma_c(2\pi)^{1/2}}\exp\{-c^2/2\sigma_c^2\}, \tag{A2}$$

so that

$$P(I)=p(c(I))\left|\frac{dc}{dI}\right|. \tag{A3}$$

The inversions implicit in (A3) can be carried out numerically. However, an accurate analytical form can be found provided that $\sigma_c x^2$ does not become too large. In this case the expressions (A1) can be expanded to give

$$I(t)\approx I_0\left|\left(1-\frac{|c|x^2}{6}+\frac{|c|^2x^4}{120}\right)^{-1}\right|, \quad c<0$$
$$=I_0\left|\left(1+\frac{|c|x^2}{6}+\frac{|c|^2x^4}{120}\right)^{-1}\right|, \quad c>0 \tag{A4}$$

so that

$$I(t)\approx I_0\left(1+\frac{cx^2}{6}+\frac{c^2x^4}{120}\right)^{-1}, \quad \forall c, \tag{A5}$$

since the expression inside the brackets is positive for real c. Since σ_c, Eq. (23), has a value of approximately 4×10^{-7}

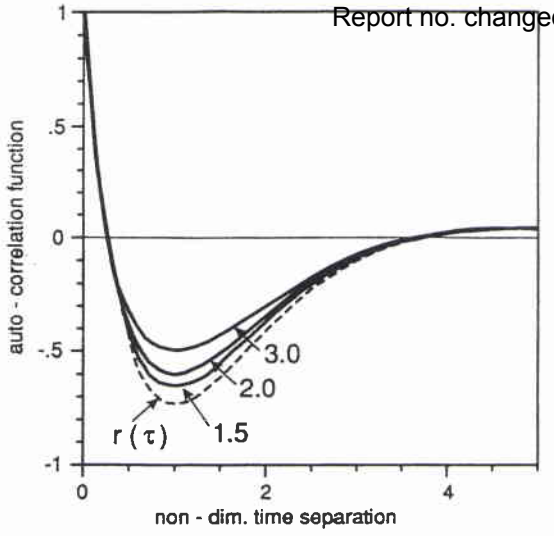

FIG. A1. $R(\tau)$ for different values of $\sigma_c x^2$ (solid lines) and the corresponding $r(\tau)$ (broken line).

and the range x of the layer traversed by the rays is less than 2 km (Fig. 1), then $|cx^2/6|$ has a maximum value of about 0.27 and the last term in the brackets of (A5) can be neglected to give

$$c=6(I_0 I^{-1}-1)x^{-2}, \tag{A6}$$

and

$$\left|\frac{dc}{dI}\right|=\frac{6I_0}{I^2x^2}. \tag{A7}$$

Using (A2)–(A7) we obtain

$$P(I)dI=[\sigma_I\sqrt{2\pi}]^{-1}I_0 I^{-2}\exp\{-(I-I_0)^2/2\sigma_I^2 I^2\}dI, \tag{A8}$$

where

$$\sigma_I=\sigma_c x^2/6. \tag{A9}$$

The method is valid for $\sigma_I \ll 1$, while our estimates show that in the present case $\sigma_I=0.27$.

We now choose I_0 so that $\langle I\rangle=1$. From (A3)

$$\langle I\rangle=\int IP(I)dI=\int I(c)p(c)dc. \tag{A10}$$

With $I(c)$ in the form (A5) the integral (A10) must be evaluated numerically. The resulting I_0 is then used in the density $P(I)$, (A8) which is shown in Fig. 13 for several values of $\sigma_c^2 x$.

For $\sigma_I \ll 1$ the expression (A5) can be expanded in powers of cx^2 to give

$$I(t)\approx\left(1-\frac{cx^2}{6}+\frac{7c^2x^4}{360}\right). \tag{A11}$$

The integral (A10) then yields, for $\langle I\rangle=1$,

$$I_0=(1+7\sigma_I^2/10)^{-1}. \tag{A12}$$

With this value of I_0 the form of $P(I)$ (A8) agrees well with the numerical results for $\sigma_c x^2 \leqslant 1.5$.

3. The scintillation index S_I^2

This quantity, defined in Eq. (11), can be evaluated using the numerical value of $\langle I\rangle$, while $\langle I^2\rangle$ is evaluated in a similar manner as

$$\langle I^2\rangle=\int I^2(c)p(c)dc. \tag{A13}$$

The resulting scintillation index is given in Table I for various values of $\sigma_c x^2$. An analytical expression for S_I^2 can be derived using the approximation (A11) for I. It is

$$S_I^2=(1+\tfrac{12}{5}\sigma_I^2)(1+\tfrac{7}{10}\sigma_I^2)^{-2}-1. \tag{A14}$$

However, this form agrees with the numerical results of Table I only for $\sigma_c x^2 \leqslant 1.5$.

4. The intensity autocorrelation function $R(t_1-t_2)$

This quantity, Eq. (13), can be evaluated in the same manner as S_I^2. Here

$$\langle I(t_1)I(t_2)\rangle=\int_{-\infty}^{\infty}\int I(c_1)I(c_2)p(c_1,c_2)dc_1\,dc_2, \tag{A15}$$

where

$$p(c_1,c_2)=[2\pi\sigma_c^2(1-r^2)^{1/2}]^{-1}\exp\{-(c_1^2-2rc_1c_2+c_2^2)/2\sigma_c^2(1-r^2)\} \tag{A16}$$

is the joint normal distribution of c_1, c_2, the curvatures at times t_1, t_2, $r(c_1, c_2)$ is the time autocorrelation function of the curvature and the $I(c)$ are given by Eq. (A5).

When $\sigma_c x^2$ is very small the expansion (A11) for $I(c)$ can be used and the expression (A15) evaluated analytically to give

$$R(t_1-t_1)=r(t_1-t_2), \tag{A17}$$

showing that the time autocorrelation of intensity is the same as that of the refractive index curvature in this limit.

The integral (A15) was evaluated numerically using the simple analytical form

$$r(\tau)=e^{-\tau}(1-4\tau+\tau^2), \tag{A18}$$

which has the same general properties as the observed autocorrelation function (Fig. 10). The resulting $R(\tau)$ is shown in Fig. 14 for several values of $\sigma_c x^2$, together with the limiting form (A17).

APPENDIX B: $R(\tau)$ FOR INTERNAL WAVES

If $A^2(\omega)$ is the power spectrum of the stochastic process $n(t)$ then $r(\tau)$, the autocorrelation function of its curvature $c(t)$, Eq. (21), is given by

$$r(\tau)=\int A^2(\omega)\cos(\omega\tau)d\omega. \tag{B1}$$

Assuming that $n(t)$ is the randomly varying acoustic refractive index due to a saturated internal wave field described by the Garrett–Munk model, the form of $A^2(\omega)$ is [Ref. 14, Eq. (25)],

$$A^2(\omega)=(f_N^2-\omega^2)^{1/2}/\omega^3, \quad f_I<\omega<f_N \tag{B2}$$
$$=0, \quad f_N<\omega<f_I,$$

where f_N, f_I are the buoyancy and inertial frequencies, respectively. The normalized autocorrelation function of $c(t)$ is then

$$R(\tau_1)=2[pq^{-2}+\tfrac{1}{2}\ln\{(1-p)/(1+p)\}]^{-1} \times\int_q^1 (1-y^2)^{1/2}y^{-3}\cos(\tau_1 y)\,dy, \tag{B3}$$

where

$$p=(1-q^2)^{1/2}, \quad q=f_I/f_N,$$
$$\tau_1=\tau f_N, \quad y=\omega/f_N. \tag{B4}$$

This function is shown in Fig. B1 for

$$f_I=1.5\times10^{-5}\ \text{Hz}, \quad f_N=1.8\times10^{-4}\ \text{Hz},$$

the values appropriate to the NAPOLI 85 experiment.[6]

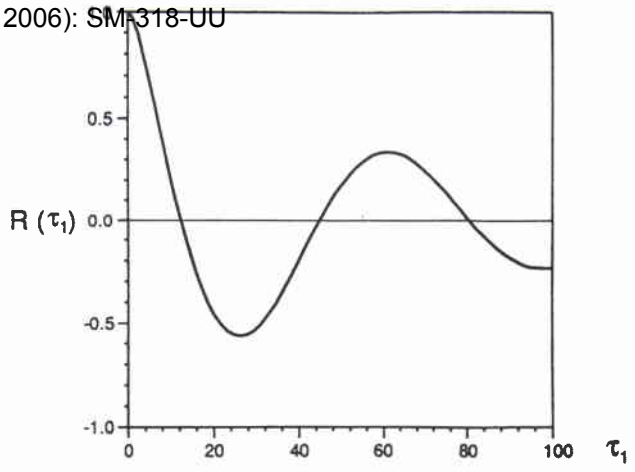

FIG. B1. The normalized time autocorrelation function of acoustic refractive index curvature $R(\tau_1)$ for a saturated internal wave field.

APPENDIX C

1. Diffraction by the intrusive layer

The model adopted for this effect is shown in Fig. C1. An additional set of coordinates (x,y,z') is introduced with origin at the effective source. The phase modulation imposed by the layer irregularities when projected on to the z_b' plane is $\psi(x')$ with autocorrelation function

$$C_\psi(x_1'-x_2')=\langle\psi(x_1')\psi(x_2')\rangle. \tag{C1}$$

The acoustic field, modulated by the layer, arriving at a point y on the vertical array at horizontal range x from the source is approximately

$$E(y,x)=(r_1r_2)^{-1}\exp\{i[k_1(r_1+r_2)+\psi(x')]\}. \tag{C2}$$

We now define a reference straight line path from the origin to v_1, the center point of the vertical array. The acoustic field reaching v_1 by this path, unmodulated by the layer, is taken as the reference, "unscattered" field. Subtraction of this from the field (C2) gives the modulated or "scattered" component. Using the fact that the slant angle ϕ and the phase modulation $\psi(x')$ are small quantities, we make the standard expansions in the exponents to obtain for the "scattered" field

$$E'(x',y)=i\psi(x')\exp\left\{i\frac{k}{2}\left[\frac{x'^2\sin^2\phi}{v_0}+\frac{(x'\sin\phi-y\cos\phi)^2}{v_1-v_0}\right]\right\}. \tag{C3}$$

The phase of the unscattered field has been taken as the reference phase and removed from that of the scattered field.

A knowledge of $E'(x,y)$ allows us to find R_{12}, Eq. (18), the spatial autocorrelation function of intensity fluctuations down the array. It is shown in Appendix D that for small intensity variations

$$R_{12}=\text{Re}\{\langle E_1'E_2'^*\rangle+\langle E_1'E_2'\rangle\}/\text{Re}\{\langle E'E'^*\rangle+\langle E'^2\rangle\}, \tag{C4}$$

where

$$E_i'=E'(x,y_i).$$

The quantities $\langle E_1'E_2'^*\rangle$ and $\langle E_1'E_2'\rangle$ are found by forming the appropriate products from (C3) and integrating over points x_i' in the layer. For this purpose we introduce the variables

$$u=x_1'-x_2', \quad V=(x_1'+x_2')/2, \tag{C5}$$
$$\zeta=y_1-y_2, \quad Z=(y_1+y_2)/2.$$

We can let $Z=0$ since C_{12} will depend only on the depth separation ζ if we confine ourselves to the vertical extent of the array. In the product $\langle E_1'E_2'^*\rangle$ the integral with respect to V can be carried out first, followed by that with respect to u, giving

$$\langle E_1E_2^*\rangle=2\pi p^{-2}C_\psi(v_0\zeta/v_1\tan\phi), \tag{C6}$$

where

$$p^2=kH\sin^2\phi,$$

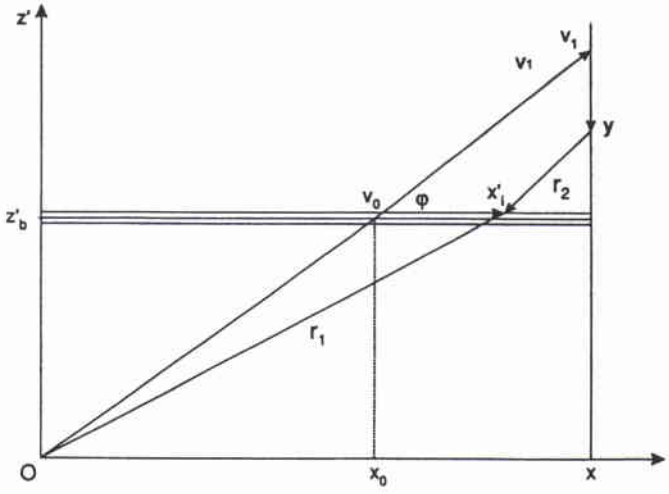

FIG. C1. The model used in calculating diffraction by the intrusive layer showing the additional set of coordinates.

$$H=\left[\frac{1}{v_0}+\frac{1}{v_1-v_0}\right]. \tag{C7}$$

In the product $\langle E_1' E_2' \rangle$ the integral with respect to V is

$$\int e^{ip^2V^2}\,dV=\sqrt{\frac{\pi}{ip^2}}, \tag{C8}$$

giving finally

$$\langle E_1' E_2' \rangle = -(\pi/ip^2)^{1/2}\int C_\psi(u)\exp\left\{ i\left[\frac{1}{4}p^2u^2 - wu\zeta + s\zeta^2\right]\right\} du, \tag{C9}$$

where

$$w=k\cos\phi\sin\phi/2(v_1-v_0),$$
$$s=k\cos^2\phi/4(v_1-v_0). \tag{C10}$$

2. The projected autocorrelation function of the layer

The goemetry of the projection is given in Fig. C2. For straight rays $x[z']$ is given by

$$x=x_i z'/z_b', \tag{C11}$$

and the phase change that accumulates along such a path is

$$\psi(x)=k\eta_2\int_{z_a'}^{z_b'} n'(x[z'],z')dz', \tag{C12}$$

when

$$C_\psi=\langle\psi(x_1)\psi(x_2)\rangle=k^2\eta_2^2\int_{z_a'}^{z_b'}\int R(g)dz'\,dz'', \tag{C13}$$

where

$$g=[(x_1z'-x_2z'')^2(z_bL_H)^{-2}+(z'-z'')^2L_v^{-2}]^{1/2}, \tag{C14}$$

and $R(g)$ is the two-dimensional spatial autocorrelation function of random structures in the intrusive layer. This function is discussed in Ref. 5 where the following empirical form was found for it by fitting the oceanographic measurements[6]

$$R(g)=\exp(-g)\{1-g/l_2+g^2/l_3^2\}. \tag{C15}$$

Here l_2, l_3 are constants ensuring the curve of best fit.

The double integral in (C13) is evaluated by first expanding $R(g)$ in terms of small displacements of z', z'' from z_a and neglecting quadratic and higher-order terms to give, in normalized form

$$C_\psi(x_1'-x_2')=\exp\{-\xi_1\}\{1-A_1\xi_1+A_2\xi_1^2-A_{3_1}\zeta_1^3+\cdots\}, \tag{C16}$$

with

$$\xi_1=|(x_1'-x_2')|(L_Hz_b'/z_a')^{-1},$$
$$A_1=[l_2^{-1}+\alpha(1+l_2^{-1})],$$
$$A_2=[l_3^{-2}+\alpha(l_2^{-1}+2l_3^{-2})], \tag{C17}$$
$$A_3=\alpha l_3^{-2},$$

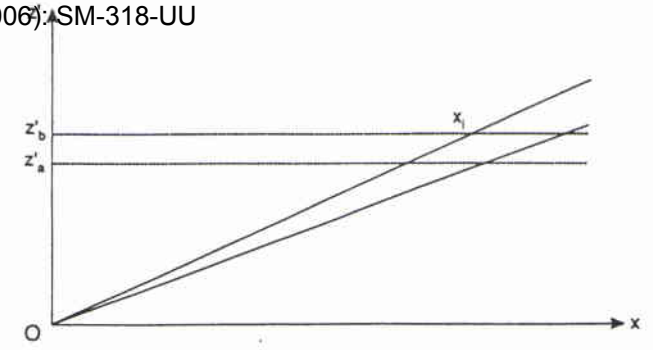

FIG. C2. Geometry used in projecting the spatial autocorrelation function of inhomogeneities in the intrusive layer.

$$\alpha=(z_b'-z_a')z_a'/2.$$

The values of the quantities in (C17) can be obtained from the estimates of z_a', z_b' for the layer, and from the results of Ref. 5 for L_H, l_2, and l_3. The angle ϕ, which determines the depth of the effective source, is estimated from the slope of the deterministic rays as they traverse the layer (Fig. 1). The correlation function (C16) is used in (C9) to give the theoretical spatial autocorrelation function of diffraction intensity fluctuations down the array. The result is shown in Fig. C3 for several values of the effective source depth.

APPENDIX D: INTENSITY AUTOCORRELATION FUNCTION

Write the acoustic field E as

$$E=E_0(1+\mathbf{a}), \tag{D1}$$

where the small "scattered" component

$$E_s=E_0\mathbf{a}. \tag{D2}$$

Then for the intensity $\mathcal{I}=EE^*$,

$$\mathcal{I}-\bar{\mathcal{I}}=E_0^2[\mathbf{a}+\mathbf{a}^*], \tag{D3}$$

where higher-order terms like $\mathbf{aa}^*$ have been neglected because of their smallness. The required normalized autocorrelation function Eq. (18) is then

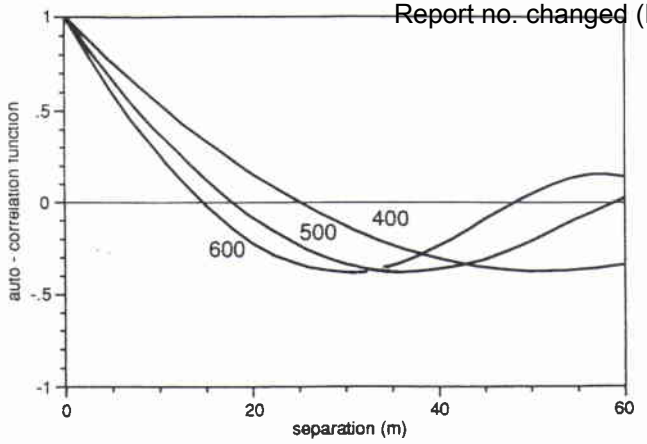

FIG. C3. Theoretical spatial autocorrelation functions of diffraction intensity fluctuations down the vertical array for different effective source depths, 400, 500, and 600 m.

$$C_{12}=\overline{(\mathscr{I}_1-\bar{\mathscr{I}}_1)(\mathscr{I}_2-\bar{\mathscr{I}}_2)}/\overline{(\mathscr{I}-\bar{\mathscr{I}})^2},$$
$$=\overline{(\mathbf{a}_1+\mathbf{a}_1^*)(\mathbf{a}_2+\mathbf{a}_2^*)}/\overline{(\mathbf{a}+\mathbf{a}^*)^2}. \quad \text{(D4)}$$

This can be rewritten in the form (C4) since the subscripts 1,2 can be interchanged.

[1]T. E. Ewart, "Acoustic fluctuations in the open ocean—A measurement using a fixed refractive path," J. Acoust. Soc. Am. **60**, 46–59 (1976).
[2]T. E. Ewart and S. A. Reynolds, "The mid-ocean acoustic transmission experiment, MATE," J. Acoust. Soc. Am. **75**, 785–802 (1984).
[3]T. E. Ewart and S. A. Reynolds, "Instrumentation to measure the depth-time fluctuations in acoustic pulses propagated through internal waves," J. Atmos. Ocean. Technol. **7**, 129–139 (1990).
[4]A. W. Ellinthorpe, "The Azores range," Tech. Doc. 4551, NUSC, New London, CT (April 1973).
[5]B. J. Uscinski, J. R. Potter, and T. Akal, "Broadband acoustic transmission fluctuations during NAPOLI '85, an experiment in the Tyrrhenian Sea; preliminary results and an arrival time analysis," J. Acoust. Soc. Am. **86**, 2, 706–715 (1989).
[6]J. R. Potter, "Fine structure in NAPOLI '85, an ocean/acoustic experiment," J. Acoust. Soc. Am. **89**(4), 1643–1655 (1991).
[7]J. R. Potter, "Oceanographic analysis of NAPOLI '85, an experiment in the Tyrrhenian Sea," Saclantcen Memorandum No. SM 234 (March 1990).
[8]L. Ju. Fradkin, "Identification of the acoustic ocean transfer function in the Tyrrhenian Sea. I: Statistical considerations," J. Acoust. Soc. Am. **87**, 1569–1576 (1990).
[9]L. Ju. Fradkin, "Identification of the acoustic ocean transfer function in the Tyrrhenian Sea. II: Physical considerations," J. Acoust. Soc. Am. **87**, 1577–1581 (1990).
[10]L. Ju. Fradkin, "A note on identification of the acoustic ocean transfer function in the Tyrrhenian Sea," J. Acoust. Soc. Am. **90**, 1678–1679 (1991).
[11]L. Ju. Fradkin, "Identification of the acoustic ocean impulse response function in the Tyrrhenian Sea," Proc. Inst. Acoust. **13**(a), 220–226 (1991).
[12]J. R. Potter, "A simple deconvolution method for NAPOLI '85," Saclantcen Memorandum, No. SM 248, October (1991).
[13]C. Macaskill and B. J. Uscinski, "Propagation in waveguides containing random irregularities: the second moment equation," Proc. R. Soc. London Ser. A **377**, 73–98 (1981).
[14]B. J. Uscinski, "Parabolic moment equations and acoustic propagation through internal waves," Proc. R. Soc. London Ser. A **372**, 117–148 (1980).

Report no. changed (Mar 2006): SM-318-UU

Document Data Sheet

NATO UNCLASSIFIED

Security Classification		Project No.
NATO UNCLASSIFIED		05
Document Serial No.	**Date of Issue**	**Total Pages**
SM-318	November 1996	20 pp.

Author(s)

T. Akal and B.J. Uscinski

Title

Broadband acoustic intensity fluctuations in the Tyrrhenian Sea

Abstract

An acoustic propagation experiment was carried out in the Tyrrhenian Sea in October 1985 in which signals from a broadband source were recorded at a range of 5 km with a vertical 62 m hydrophone array over a period of 5 days. The experiment, named 'NAPOLI 85', was designed to investigate the transfer function of the ocean medium over an acoustic frequency range from 250–2000 Hz as a function of time and position down the vertical array. This paper treats the ocean transfer function in both the time and frequency domains for the lower refracted path. The intensity fluctuations down the array at an acoustic frequency of 1 kHz are presented for the 5 days. Large fluctuations occur simultaneously over the whole extent of the array, and these can be explained by refractive effects in an intrusive later. There are also weak spatial variations down the array arising from diffractive effects in the layer. The physical mechanisms causing the time variations in the layer are not yet understood.

Keywords

Tyrrhenian Sea – propagation – sound ribbons – scattering

Issuing Organization

North Atlantic Treaty Organization
SACLANT Undersea Research Centre
Viale San Bartolomeo 400, 19138 La Spezia, Italy

[From N. America: SACLANTCEN (New York) APO AE 09613]

Tel: +39 (0)187 540 111
Fax:+39 (0)187 524 600

E-mail: library@saclantc.nato.int

NATO UNCLASSIFIED

Initial Distribution for SM-318

SCNR for SACLANTCEN		*National Liaison Officers*	
SCNR Belgium	1	NLO Canada	1
SCNR Canada	1	NLO Denmark	1
SCNR Denmark	1	NLO Germany	1
SCNR Germany	1	NLO Italy	2
SCNR Greece	2	NLO Netherlands	1
SCNR Italy	1	NLO UK	3
SCNR Netherlands	1	NLO US	4
SCNR Norway	1		
SCNR Portugal	1		
SCNR Spain	1		
SCNR Turkey	1		
SCNR UK	1		
SCNR US	2		
French Delegate	1		
SECGEN Rep. SCNR	1	Total external distribution	34
NAMILCOM Rep. SCNR	1	SACLANTCEN Library	26
SACLANT	3	Total number of copies	60